Center for Turbulence Research
Proceedings of the Summer Program 1994

Homogeneous turbulence subjected to mean flow with elliptic streamlines

By G. A. Blaisdell[1] AND K. Shariff[2]

Direct numerical simulations are performed for homogeneous turbulence with a mean flow having elliptic streamlines. This flow combines the effects of rotation and strain on the turbulence. Qualitative comparisons are made with linear theory for cases with high Rossby number. The nonlinear transfer process is monitored using a generalized skewness. In general, rotation turns off the nonlinear cascade; however, for moderate ellipticities and rotation rates the nonlinear cascade is turned off and then reestablished. Turbulence statistics of interest in turbulence modeling are calculated, including full Reynolds stress budgets.

1. Introduction

1.1. Motivation

There are many important reasons for studying the elliptic streamline flow. This flow contains the effects of both rotation and strain and is therefore similar to the mean flow in a vortex strained in the plane perpendicular to its axis. Such flows provide insight into fundamental vortical interactions within turbulence, and the instability caused by the strain has been proposed as a universal mechanism for energy transfer from large scales to small scales (Pierrehumbert 1986).

A strained vortex also occurs in airplane wakes, in which each wingtip vortex induces a strain field on the other. The strain field can affect the stability of these vortices and thereby their turbulent structure downstream. The ability to understand and predict the turbulent structure of the vortices is important to the wake hazard problem which is of major concern for the safety of commercial aircraft.

Another example of a flow with the combined effects of rotation and strain is the outer core of the earth's interior. The electrically conducting fluid in the outer portion of the earth's core rotates with the earth but is also strained by tidal forces. A large-scale secondary flow results, which has been proposed as the cause of the magnetic field (Malkus & Berry 1988). Additional examples are flow in fluid-filled satellites and in rectangular cavities.

The elliptic streamline flow is also a good test case for turbulence models for rotating flows. It has an added complication beyond that of pure rotation, but it is still a basic flow. The additional strain rate is present in most practical engineering flows and, therefore, is a necessary effect for turbulence models to capture. The behavior of the turbulent statistics shown in section 3 are quite complex, and thus the elliptic streamline flow presents a challenging case for turbulence modelers.

1 Purdue University
2 NASA Ames Research Center

1.2. Background

The linear stability of elliptic streamline flow was studied by Pierrehumbert (1986), Bayly (1986), and Waleffe (1990), who performed inviscid stability analyses using different methods. For circular streamlines (pure rotation) there are no unstable modes, while for elliptic streamlines a band of unstable modes exists in which the growth rate depends on the polar angle of the wavenumber vector. The band of unstable angles increases in width for increasing ellipticity of the streamlines. Also, the growth rate of the unstable modes is independent of the magnitude of the wavenumber vector. Therefore, arbitrarily small three-dimensional fluctuations can be created by an instability of a basic two-dimensional flow. Pierrehumbert suggested that this might be a mechanism for the cascade process in turbulent flows.

The effects of viscosity were studied by Landman & Saffman (1987). The growth rate of the instabilities is modified by viscosity so that the growth rate is no longer independent of the magnitude of the wavenumber vector. They found a high wavenumber cut-off of the instability. However, there is no low wavenumber cut-off, and arbitrarily large scales are unstable. This fact has important implications for doing numerical simulations of this flow, which are discussed below.

An interesting experiment corresponding to elliptic streamline flow was done by Malkus (1989). A tank with moving flexible walls was used to create a flow with elliptic streamlines. He observed a collapse phenomenon in which the two-dimensional flow suddenly breaks down into three-dimensional small-scale motions. Waleffe (1990) studied the stability of the enclosed elliptic flow and suggested the collapse phenomenon is due to nonlinear interactions in which the mean flow is altered. Although the collapse is observed in a confined flow, there is some evidence that a similar phenomenon may occur in one of the homogeneous turbulence simulations discussed below.

Lundgren & Mansour (1991) investigated the stability of a vortex in a rectangular domain. This flow is very similar to the elliptic streamline flow and displays a similar instability. However, their flow has a mean velocity which decays in time, and their flow is inhomogeneous. These two factors introduce additional complicating effects and make gathering turbulence statistics difficult because of the low statistical sample that is available. The elliptic streamline flow and its instability is also related to the instability of a strained, finite-sized vortex with uniform vorticity studied by Widnall *et al.* (1974) and others.

An experiment which was designed to correspond to the homogeneous elliptic streamline flow was performed by Benoit (1992). He investigated grid generated turbulence created by a rotating grid and then passed through a specially designed diffuser with elliptic cross-sections. Benoit also analyzed the flow using linear rapid distortion theory. We have not had a chance to compare his results with those of the current simulations; however, such a comparison is planned for future work.

There has been a considerable amount of work done on the stability of the elliptic streamline flow. However, there has not been any direct numerical simulation of the homogeneous elliptic flow. With the use of direct numerical simulation, the nonlinear development of the flow and the fully turbulent state can be examined.

1.3. Objectives

The objectives of this work are to perform a preliminary investigation of the elliptic streamline flow for the fully turbulent case and to provide statistics for comparison with turbulence models. One of the issues to be investigated is whether the linear instability modes grow to dominate the flow even in the presence of large initial disturbances. Whether this is the case is dependent on the governing parameters. For the elliptic streamline flow the governing parameters are: (1) the ratio of the rotation rate to the strain rate, which gives the aspect ratio of the elliptic streamlines, (2) the ratio of a mean flow time scale, such as the rotation rate, to the turbulence time scale, and (3) the turbulent Reynolds number. One major objective is to study the effect of these various parameters. However, in this preliminary study we have not been able to cover the full parameter space.

Another issue has to do with the long term behavior of the turbulence. Does the turbulence grow continually, eventually decay, reach an asymptotic stationary state, or grow and decay in a periodic fashion? The linear theory would suggest exponential growth. The possibility of an asymptotic stationary state is suggested by the related flow of homogeneous rotating shear flow (Bardina *et al.* 1983, and Speziale & Mac Giolla Mhuiris 1989), in which case there seems to be the possibility of obtaining a state in which the turbulent kinetic energy does not grow or decay. In rotating shear flow the direction of strain is fixed in the rotating frame of reference, while in elliptic streamline flow the direction of strain is fixed in the stationary frame of reference. This difference is very important. One consequence of this difference is that for elliptic streamline flow a fluid element is periodically strained as it rotates around an elliptic streamline. This periodic straining of a fluid element might cause the turbulence to grow and then decay in a periodic fashion.

Turbulence statistics, including full Reynolds stress budgets, have been calculated during each of the simulations. The behavior of these statistics is discussed below; however, a comparison with turbulence models has not been done at this time.

2. Governing equations

Consider homogeneous turbulence with the mean flow

$$U_i = U_{i,j}x_j, \quad U_{i,j} \equiv \begin{pmatrix} 0 & 0 & -\gamma-\epsilon \\ 0 & 0 & 0 \\ \gamma-\epsilon & 0 & 0 \end{pmatrix}, \tag{1}$$

which describes a one-parameter family of streamline patterns in the x-z plane (the other parameter sets the strength of the flow). The case $\gamma = 0$ corresponds to pure strain with two principal directions at $\pm 45°$ relative to the x-axis while $0 < |\gamma| < |\epsilon|$ gives vortical strain dominated flows with hyperbolic streamlines, their asymptotes being shallower or steeper than the pure strain case according as $(\epsilon-\gamma)/(\epsilon+\gamma) < 1$ or > 1. The limit $|\epsilon| = |\gamma|$ is pure shear. The case $\epsilon = 0$ corresponds to pure rotation while $0 < |\epsilon| < |\gamma|$ gives vortical rotation dominated flows with geometrically similar elliptic streamlines with aspect ratio $E \equiv \sqrt{(\gamma+\epsilon)/(\gamma-\epsilon)}$. This case is depicted in Fig. 1.

The code shear_i, developed by Dr. R. S. Rogallo (of Los Altos Hills, Calif.) to run on the Intel parallel computers at NASA Ames for the case of pure shear and employing a subset of the techniques described in Rogallo (1981), was modified to treat the above cases. The xz plane was chosen as the plane of deformation to minimize disruption to the code. The program uses the second-order Runge-Kutta scheme to time-advance the Fourier transformed Navier-Stokes equation (notation will be explained momentarily):

$$\frac{d}{dt}(F\widehat{u}_i) = F\left\{\Pi^{(2)}_{ij}U_{j,m}\widehat{u}_m - i\Pi^{(1)}_{ij}k_m\widehat{u_j u_m}\right\} \tag{2}$$

Due to the use of coordinates that deform with the mean flow, the k_i in Eq. (2) represent time-dependent physical wavenumbers:

$$k_i = k'_j B_{ji}(t), \quad \dot{B}_{ij} = -B_{ik}U_{k,j}, \tag{3}$$

while hats denote the three-dimensional Fourier transform with respect to computational wavenumbers k'_i. Space discretization is implied by the restriction of k'_i to integers $-M/2 \le k'_i \le M/2$; homogeneity is realized when there is a sufficiently large range of small wavenumbers with energy tending to zero. The symbol $\Pi^{(n)}_{ij} \equiv \delta_{ij} - nk_ik_j/k^2$ with $n = 1$ is the projector applied to the Navier-Stokes equation to eliminate pressure; a slightly different projector, $\Pi^{(2)}_{ij}$, appears in the linear term due to an additional contribution from the time derivative term in deforming coordinates. The aliasing error concomitant with the pseudo-spectral evaluation of $\widehat{u_j u_m}$ is controlled (but not exactly eliminated) by a combination of phase shifting and spherical truncation in which modes with $k' > 2(M/3)^2$ are discarded upon return to wavenumber space. The viscous integrating factor F, satisfying $(1/F)dF/dt = +\nu k^2(t)$, is obtained analytically. Since in the linearized limit exact time integration of (2) is not possible (or at least not trivial (Waleffe 1990)), the present version of the program does not treat the rapid distortion limit exactly. Rather, the time step is chosen to be the more restrictive one obtained from the mean flow and the non-linear term. For pure shear the flow-field can be re-meshed to prevent extreme distortion of the computational domain. In the elliptic flow, however, a fluid element undergoes time-periodic shearing and straining, and rather than tackle the corresponding re-meshing problem, small enough ellipticities are considered so that the minimum interior angle of the element, $\theta_{\min} = \tan^{-1}\left[2E/(E^2-1)\right]$, does not become too small (for the largest case of $E = 2$ considered, $\theta_{\min} = 53°$).

The code was tested for: (i) The linear inviscid and viscous behavior of a single Fourier mode compared with the results of Landman & Saffman (1987) (ii) Pure rotation (Mansour *et al.* 1991, $Ro = 0.247$, their Fig. 2*a*) (iii) Pure shear (Rogers *et al.* 1986, Case C128U).

3. Simulations and results

One of the objectives of this study is to examine the effect of the relative time scales of the mean flow and the turbulence and the effect of the elliptic streamline

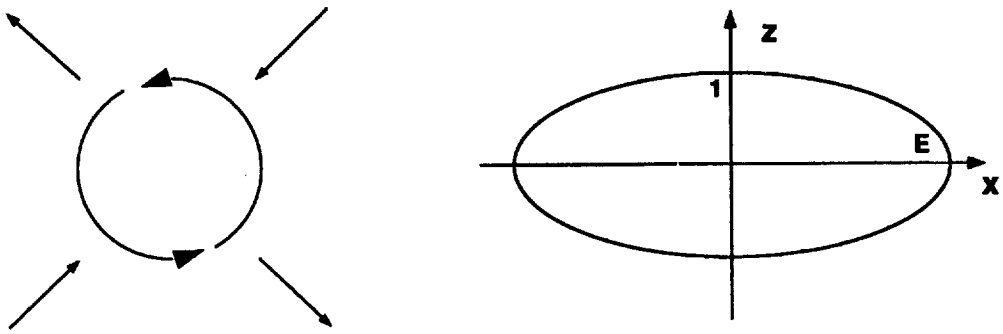

FIGURE 1. (a) Schematic view of combination of rotation and strain. (b) Elliptic streamline. (The direction of the arrows corresponds to $\gamma > 0$ and $\epsilon > 0$.)

Table 1. Initial condition and run parameters for the simulations.

Case	E	Ro	Re_{T_0}	grid	k_p
A	1.1	1.46	51	128^3	18
B	1.1	0.247	51	128^3	18
C	1.1	0.0037	51	128^3	18
D	2.0	0.247	51	128^3	18
D′	2.0	0.247	51	256^3	36

aspect ratio. We were guided in our choice of parameters by the pure rotation DNS of Mansour *et al.* (1991). Following them we define a Rossby number as $Ro = \varepsilon/(\Omega k)$, where ε is the dissipation rate of turbulent kinetic energy per unit mass, $\Omega \equiv \sqrt{\gamma^2 - \epsilon^2}$ is the rotation frequency, and k is the turbulent kinetic energy per unit mass. The period for a fluid element to traverse an elliptical streamline is $T = 2\pi/\Omega$. This is also the period of oscillation for the wavenumber vectors in the linear stability analyses. The Rossby number, Ro, is the ratio of the time scale of the mean flow and the time scale of the turbulence. Mansour *et al.* have considered a range of Rossby numbers. The general effect of increasing rotation rates is to shut off the nonlinear cascade process. We have chosen to use three of their values of Ro: a case with weak rotational effects ($Ro = 1.46$), moderate rotational effects ($Ro = 0.247$), and strong rotational effects ($Ro = 0.0037$). The elliptic streamline flow has the additional parameter of the aspect ratio of the elliptic streamlines, E. We have chosen to use $E = 1.1$ for most of the runs in order to remain close to the case of pure rotation. In one case we use $E = 2.0$ to see the effect of larger aspect ratio. The parameters for the simulations to be presented are shown in table 1.

The initial conditions for the simulations were obtained in the same way as those

of Mansour *et al.* (1991). An initial energy spectrum was specified of the form

$$E(\kappa) = \kappa^4 \exp(-2(\kappa/\kappa_p)^2) \quad , \tag{4}$$

where κ_p is the location of the peak in the spectrum. For most of the runs κ_p was chosen to be 18 and the computational grid was 128^3. The flow field was then evolved as decaying isotropic turbulence until it became fully developed as measured by the velocity derivative skewness obtaining a steady value near -0.5 and the turbulent kinetic energy displaying algebraic decay with a constant decay rate. This developed flow field was then used as initial conditions for the elliptic flow runs. The simulations presented here do not match the Reynolds number of Mansour *et al.* We attempted to do so, but were confronted with the difficulty that, with the elliptic streamline flow, the large scales gain energy and quickly outgrow the computational domain. This problem does not occur for the pure rotation case where the turbulence simply decays. As a result, we found it necessary to change our initial conditions to make the computational domain larger relative to the initial integral scales of the turbulence. Because of the corresponding loss of resolution in the small scales, we reduced the Reynolds number. All of the elliptic flow simulations presented here have an initial turbulent Reynolds number $Re_T = q^4/(\varepsilon\nu) = 51$ ($Re_t = k^2/(\varepsilon\nu) = 12.75$ following the notation of Mansour *et al.*). This compares to the value $Re_T = 109$ ($Re_t = 27.24$) for the 128^3 simulations of Mansour *et al.* With the peak in the initial spectrum pushed to higher wavenumbers, we were able to run the simulations further in time before the turbulence outgrew the computational domain. Simulation D′ is the same as case D except that a 256^3 grid was used and $k_p = 36$ so that the computational domain is twice as large relative to the turbulence length scales. The larger domain allowed the simulation to be carried out further in time and also provided a check on the effect of the domain size on case D.

3.1. Case A

Case A has an initial Rossby number of 1.46, which indicates that the effect of rotation is relatively weak. Since the dominant effect of rotation on the turbulence is to suppress the nonlinear cascade, it is useful to have a measure of the nonlinear transfer of energy from large scales to small scales. Mansour *et al.* (1991) used a generalized skewness defined by

$$S = -\frac{6\sqrt{15}}{7} \frac{\int \kappa^2 T(\kappa)\, d\kappa}{\left(\int \kappa^2 E(\kappa)\, d\kappa\right)^{3/2}} \quad , \tag{5}$$

where κ is the magnitude of the wavenumber vector, $E(\kappa)$ is the three-dimensional energy spectrum, $T(\kappa)$ is the transfer spectrum, and the numerical prefactor is such that for isotropic turbulence $S = -0.5$. The evolution of S for case A is shown in Fig. 2b. S begins near -0.5 since the initial conditions consist of decaying isotropic turbulence. Within one period the skewness falls to below -0.1, indicating that the nonlinear cascade has been suppressed considerably. The reduction in S seems far

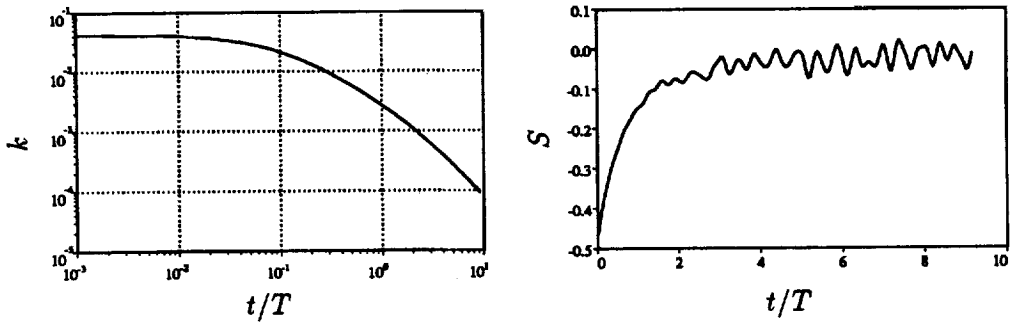

FIGURE 2. (a) Turbulent kinetic energy, k, for case A. (b) Skewness, S, for case A.

greater than that for the corresponding pure rotation case of Mansour *et al.* , for which S is reduced to -0.4. However, the extent of the two simulations is not the same; the final time for the simulation by Mansour *et al.* is $t/T = 0.25$.

Because the rotation rate in case A is relatively low and the ellipticity is small, the production of turbulent kinetic energy is also low. Dissipation dominates production during the course of the simulation so that the turbulence decays, as shown in Fig. 2a. However, since the flow is linearly unstable and the minimum unstable wave length fits within the computational domain, we believe that the turbulence must eventually grow. For this case the growth rates are very low, and so it would take a very long time to observe growth. A period of decay followed by growth is observed in case B.

3.2. Case B

Case B has an initial Rossby number of 0.247. Because of the higher production rate compared to case A, the growth in turbulent kinetic energy is observed within a reasonable period of time. The turbulent kinetic energy history is shown in Fig. 3a. There is a period of decay followed by exponential growth (as indicated by the linear increase on a semilog plot). The skewness for case B is shown in Fig. 3b. The rotation causes S to decrease to -0.2 very quickly; S then slowly decays to near zero. At later times S becomes periodic with an increasing amplitude. The period of oscillation corresponds to half the period, T, for a fluid element to traverse an elliptic streamline; the period of oscillation is also the period of the strain field relative to a frame of reference rotating with a fluid element.

The exponential growth in the turbulent kinetic energy, the suppression of nonlinear processes, and the periodic behavior indicate that the fluctuations are likely dominated by the linear instability modes. The linear analysis of Bayly shows the modes that are unstable lie in a narrow band depending on the polar angle measured from the rotation axis of the wavenumber vector. An angular spectrum, $E(\theta)$, which gives the energy as a function of angle, is shown in Fig. 4 at the final time of simulation B. The spectrum is plotted as a function of $\cos\theta$ so that an isotropic field will give a uniform distribution. The linear theory predicts a small band of unstable modes near $\theta = 2\pi/3$ or $\cos\theta = 1/2$. This is exactly what is seen in Fig. 4. So, for case B the fluctuations are clearly dominated by the linear instability modes.

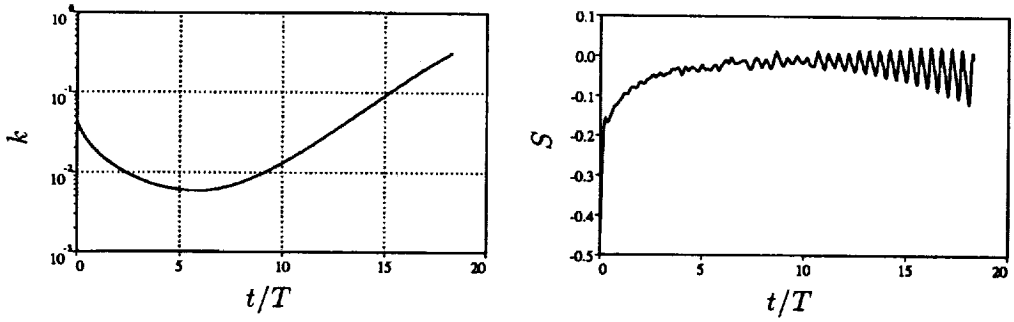

FIGURE 3. (a) Turbulent kinetic energy, k, for case B. (b) Skewness, S, for case B.

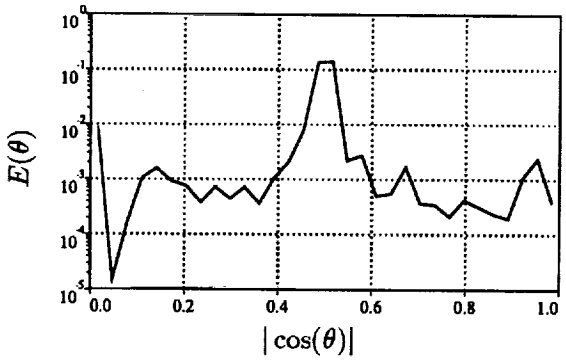

FIGURE 4. Angular energy spectrum, $E(\theta)$, for case B.

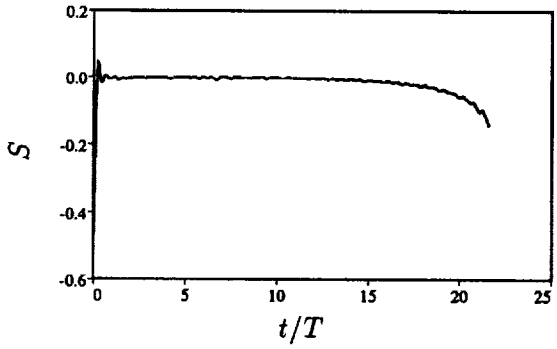

FIGURE 5. Skewness, S, for case C.

Based on the increasing amplitude of the oscillations in S shown in Fig. 3b, one might expect that nonlinear processes would increase and eventually the flow would become fully turbulent. To determine if this is the case would require a much larger computational domain so that the simulation could be carried further in time. Perhaps with a different choice of parameters, such an evolution could be observed within a time that is computationally affordable.

3.3. Case C

Case C has the lowest Rossby number, $Ro = 0.0037$, indicating very strong rotation effects. In the simulations of Mansour *et al.* the nonlinear cascade is almost completely shut off as S is nearly zero. The history of S for case C is shown in Fig. 5. S decays very quickly and remains nearly zero until the last portion of the simulation when the nonlinear processes start becoming more important. The behavior of S is similar to that in case B, and again it would be interesting to be able to continue the simulation to watch the restoration of the nonlinear cascade. The angular spectrum, $E(\theta)$, for case C (not shown) is very similar to that of case B. Therefore, both flows are dominated by the linear instability modes. The evolution of the turbulent kinetic energy for case C (not shown) also indicates exponential growth of the turbulence, however with negligible decay at early times.

3.4. Cases D and D'

Case D was done to see the effects of a larger aspect ratio of the elliptic streamlines. The aspect ratio is $E = 2$ and the initial Rossby number is $Ro = 0.247$, which is the intermediate value of the three considered. Because the large scales grow to fill the computational domain, we checked the adequacy of the domain size by running simulation D', which has a 256^3 grid and a domain size twice as large as that for case D. The results of the two simulations are compared below.

The turbulent kinetic energy for case D grows, but does not seem to grow exponentially. The growth seems to be more algebraic as indicated in Fig. 6a, which shows linear growth on a log-log plot. The exponent for the growth rate is close to 4. The two simulations agree very well, which indicates that the domain size is adequate up to the point where the simulations were terminated.

The skewness for cases D and D' are shown in Fig. 6b, and again they agree very well — the small differences between the simulations are due to differences in the initial, isotropic flow fields. The evolution of S displays some interesting behavior. At early times the rotation suppresses the nonlinear cascade and S is reduced to below -0.2. Then the nonlinear cascade seems to be reestablished as S grows back to -0.4. At later times S displays oscillations of period $T/2$ and seems to be decreasing in magnitude. The presence of the nonlinear cascade indicates that the fluctuations are not dominated by the linear instability modes. This is also seen in the angular spectrum which is presented in Fig. 7. The fluctuations are broad-band, while the linear stability analysis predicts that a limited band of modes are destabilized, although the band of modes is considerably broader for $E = 2.0$ than for $E = 1.1$ as in case B. (The picture presented by the angular spectrum is not completely clear because the spectra computed during the simulations used the physical wavenumber vectors to define the spectra, while the linear theory is based on the computational wavenumber vectors. Therefore, in order to make a valid comparison with the linear theory, the spectra subroutine must be modified and the simulations rerun.)

The behavior of S shown in Fig. 6b at later times brings up some interesting questions. Is the nonlinear cascade process being periodically turned on and off? If so, is this related to the collapse phenomenon observed in the experiments of

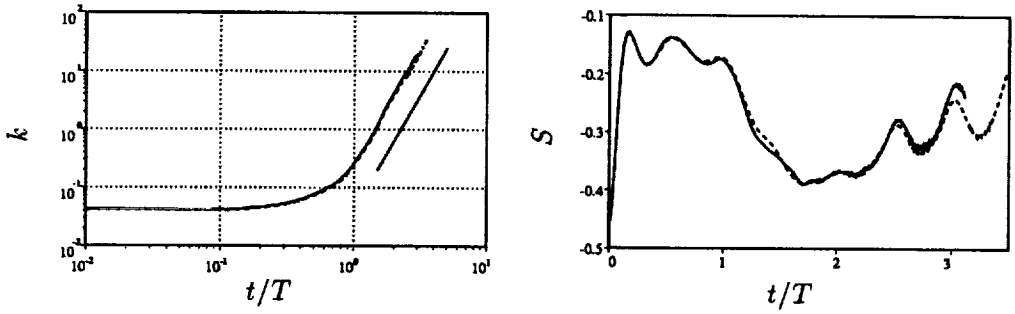

FIGURE 6. (a) Turbulent kinetic energy, k, and (b) skewness, S, for cases D, ——, and D', ---- . (The line for t^4 is shown for reference.)

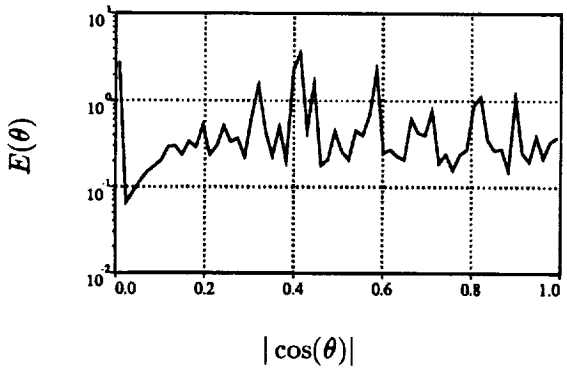

FIGURE 7. Angular energy spectrum, $E(\theta)$, for case D' at the final time of the simulation.

Malkus in which three-dimensional turbulence suddenly appears, or is this a different phenomenon? Does the skewness stay at large values, go back to zero (and then return), or oscillate about some intermediate value?

To be able to answer some of these questions we need to be able to run the simulations further in time. However, the difficulty in doing so is that the large length scales grow in amplitude and eventually dominate the flow so that the computational domain size becomes inadequate. The comparisons shown above between cases D and D' seem to indicate that the domain size for case D is adequate at least up to the time when the simulation was terminated. However, consideration of the radial, three-dimensional energy spectrum shows that even case D' has run out of box size by the end of the simulation. Fig. 8 shows the evolution of $E(\kappa)$ for case D'. The energy in the large scales steadily rises and the peak in the spectrum moves to the low wavenumbers. By the end of the simulation, the peak in the spectrum has run into the low wavenumber limit of the box. Also note that at the final time the high-wavenumber end of the spectrum seems to show some lack of small-scale resolution. The Reynolds number increases greatly during the course of the simulation, and by the end of the simulation the range of length scales is too great to be

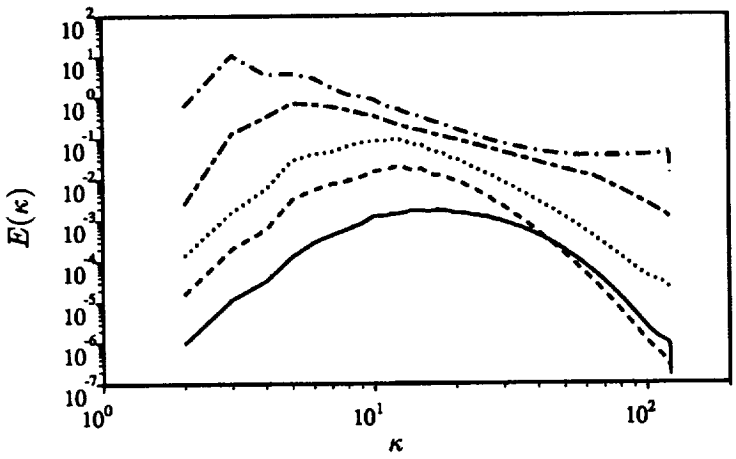

FIGURE 8. Radial energy spectra, $E(\kappa)$, for case D′. ——— , $t/T = 0.0$; ---- , $t/T = 1.02$; ····· , $t/T = 1.52$; —·— , $t/T = 2.31$; —·— , $t/T = 3.50$.

captured using 256^3 grid points. In order to carry the simulations further in time, more grid points are needed. It is feasible to perform 512^3 simulations; however, even this size grid would soon be outgrown. In order to overcome these difficulties, large-eddy simulation (LES) can be used so that high Reynolds numbers can be achieved without fully resolving the small length scales. This will allow more grid points to be used to capture the large length scales. We should also investigate the parameter space further to see if a higher aspect ratio, E, would produce similar behavior in a shorter time.

3.5. Implications for modeling

One of the goals of this study is to provide insight for turbulence modeling of rotating flows. To this end Reynolds stresses and the full Reynolds stress budgets were computed during the course of the simulations. While we have not been able to analyze the behavior of the Reynolds stresses fully, there are some observations we can make. We will discuss results from cases B and D′, since the results from these cases are the most interesting.

3.5.1 Case B

The history of the Reynolds shear stress, $R_{13} = \overline{u_1' u_3'}$, is shown in Fig. 9 for case B. This case is dominated by the linear instability modes, and oscillations of period $T/2$ are clearly seen on top of the exponential growth. This is not inconsistent with the Floquet behavior of a single unstable Fourier mode according to linear analysis (Bayly 1986), which predicts that at late times the behavior should be T-periodic but modulated by a growing exponential. The deviation from exponential growth towards the end of the simulation reflects the behavior of other indicators of nonlinearity, namely, skewness (Fig. 3b) and slow pressure-strain (Fig. 10). An interesting point is that whereas the turbulent kinetic energy shown in Fig. 3 is relatively smooth, oscillations appear in the Reynolds stresses, representing inter-component transfer of energy.

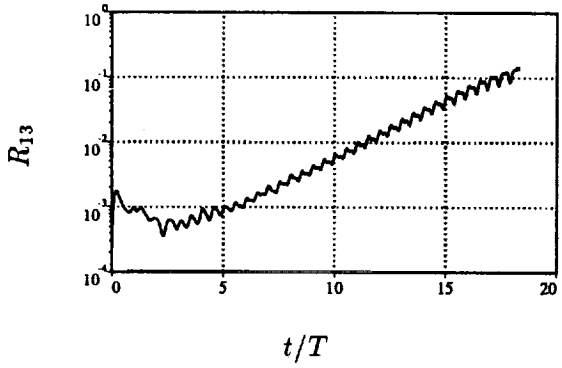

FIGURE 9. History of the Reynolds shear stress, R_{13}, for case B.

The Reynolds stress equations for homogeneous turbulence are (Reynolds 1987)

$$\frac{\overline{D}R_{ij}}{Dt} = P_{ij} + O_{ij} + T_{ij} - D_{ij} \quad , \tag{6}$$

where P_{ij} is the production term, O_{ij} is the kinematic rotation term, T_{ij} is the pressure-strain term, and D_{ij} is the dissipation rate tensor. The pressure-strain tensor is split into two parts, T^r_{ij} the rapid pressure-strain, and T^s_{ij} the slow pressure-strain. The Reynolds stress budgets for case B are shown in Fig. 10 for the 1-3 component. As a check, the sum of all the terms on the right hand side of Eq. (6) are compared to the time derivative of the Reynolds stresses, which was computed separately using the time history of the Reynolds stresses. The two terms compare very well, showing that the budgets are balanced. The dominant terms are the pressure-strain term, T_{ij}, and the kinematic rotation term, O_{ij}: they are of opposite sign and tend to partly cancel. The pressure-strain is dominated by the rapid (linear) part. The production term is important and much larger than the dissipation term, D_{ij}. Since the linear terms — rapid pressure-strain, kinematic rotation, and production — dominate, case B should be well described by the linear analysis (i.e. rapid distortion theory).

In order to get a better understanding of the turbulence structure, it is useful to consider the invariants of the Reynolds stress anisotropy tensor and various other tensor quantities. The Reynolds stress anisotropy tensor is defined as $b_{ij} = R_{ij}/q^2 - 1/3\delta_{ij}$. By definition the trace of b_{ij} is zero. The second and third invariants are $II_b = -\frac{1}{2}b_{ij}b_{ji}$ and $III_b = \frac{1}{3}b_{ij}b_{jk}b_{ki}$. The invariant map (Lumley 1978) for case B is shown in Fig. 11a. All physically realizable turbulence must lie within the triangular-shaped marked region. The left boundary corresponds to flow through an axisymmetric contraction, which would have vortex lines pulled all in one direction; the right boundary corresponds to flow through an axisymmetric expansion, which would flatten vortex lines into pancakes; and the origin corresponds to isotropic flow. From the figure it appears that the state of the turbulence changes periodically as the fluid element revolves around the elliptical streamline.

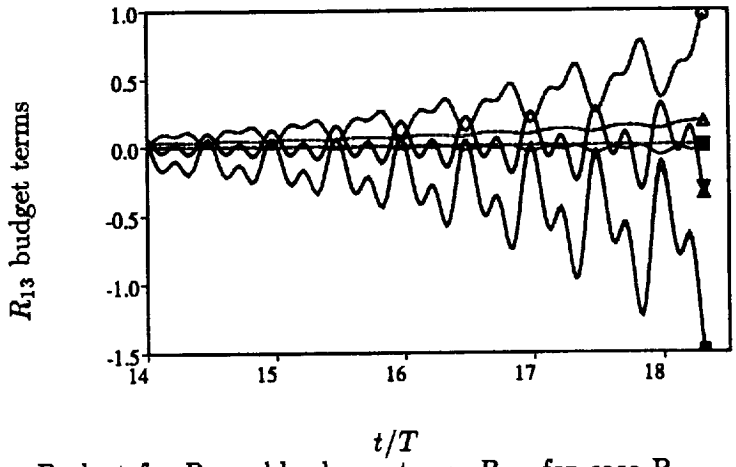

FIGURE 10. Budget for Reynolds shear stress, R_{13}, for case B. —— △ , Sum of all terms on the right hand side; —— ▽ , dR_{ij}/dt; ---- △ , P_{ij}; ---- ▽ , $-D_{ij}$; ---- ○ , O_{ij}; ····· + , T_{ij}; ····· □ , T^s_{ij}; ····· ■ , T^r_{ij}. (Since the total pressure-strain is nearly the rapid part, the symbol, ■ , lies over the + symbol.)

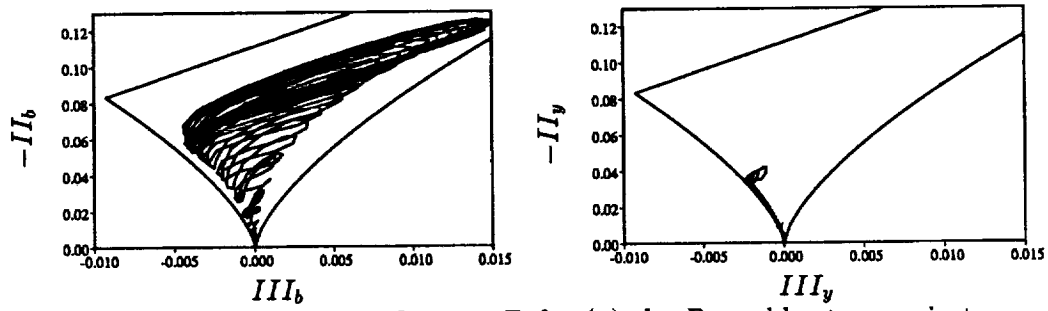

FIGURE 11. Invariant maps for case B for (a) the Reynolds stress anisotropy tensor, and (b) the structure dimensionality anisotropy tensor.

Invariant maps for the dissipation tensor and the vorticity correlation tensor are very similar to those for the Reynolds stress tensor shown in Fig. 11a. Another quantity of interest is the structure dimensionality tensor introduced by Reynolds (1989). For homogeneous flows it is most easily defined in wave space as

$$Y_{ij} = \int \frac{\kappa_i \kappa_j}{\kappa^2} E_{nn}(\vec{\kappa})\, d\vec{\kappa} \quad , \tag{7}$$

where $E_{ij}(\vec{\kappa})$ is the velocity spectrum tensor. The invariant map for the corresponding anisotropy tensor is shown in Fig. 11b, and it displays a much different behavior than for the Reynolds stress tensor. The invariants hug the left boundary and then deviate near the end of the simulation. A simulation not presented here, which had $E = 1.1$, $Ro = 0.116$, and $Re_T = 115$, had the invariants hugging the right boundary of the anisotropy map. So, there does not seem to be a special preference for the left boundary of the invariant map for the elliptic streamline flow. At this

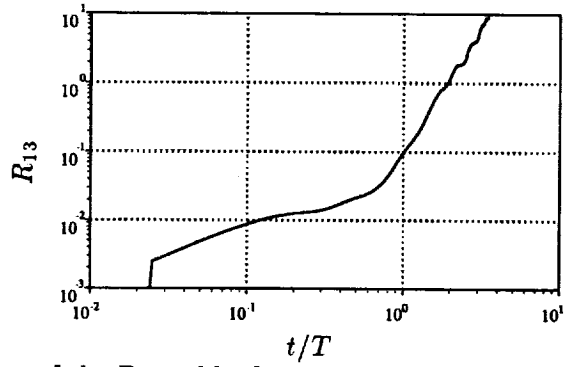

FIGURE 12. History of the Reynolds shear stress, R_{13}, for case D′.

point we are not sure what this behavior implies about the vortical structure of the turbulence.

3.5.2 Case D′

The history of the Reynolds shear stress for case D′ is shown in Fig. 12. It is not as oscillatory as for case B and and has oscillations in slope rather than magnitude. As for case B, the turbulent kinetic energy shown in Fig. 6 does not display the oscillations observed in individual Reynolds stress components. The budget for R_{13} is shown in Fig. 13. For case D′ all the terms in the Reynolds stress equations are important. The linear terms are large, but the nonlinear terms — the slow part of the pressure-strain and the dissipation rate — are significant. This would be a good test case for comparison with predictions from turbulence models.

The invariant maps of the Reynolds stress anisotropy tensor and the structure dimensionality anisotropy tensor are shown in Fig. 14. The invariants of the Reynolds stress tensor do not seem to follow a recognizable pattern, except that near the end of the simulation they oscillate in a region near the left boundary of the invariant map. The invariants of the structure dimensionality tensor remain near the origin. They oscillate once along the left boundary of the invariant map and then oscillate along the right boundary. Again, we are not sure what this behavior implies about the vortical structure of the turbulence.

4. Conclusions

Preliminary calculations of homogeneous turbulence subjected to mean flow with elliptic streamlines have been performed. The cases considered include a series of three runs with a low aspect ratio of the elliptical streamlines and which span a range of Rossby numbers. A fourth case was done with moderate values of aspect ratio and Rossby number; this case shows the most interesting results.

The case with a low aspect ratio and a high Rossby number (low rotation rate) simply decays. The other two low aspect ratio simulations show exponential growth of the turbulent kinetic energy in agreement with the linear theory. These simulations are dominated by linear effects. Examination of the turbulence cascade, using a generalized skewness, shows that the nonlinear transfer is greatly reduced

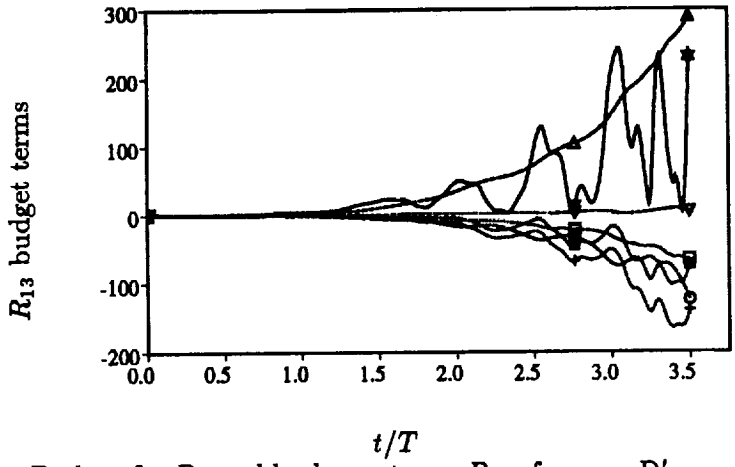

FIGURE 13. Budget for Reynolds shear stress, R_{13}, for case D'. —— △ , Sum of all terms on the right hand side (times ten); —— ▽ , $10dR_{ij}/dt$; ---- △ , P_{ij}; ---- ▽ , $-D_{ij}$; ---- ○ , O_{ij}; ····· + , T_{ij}; ····· □ , T^s_{ij}; ····· ■ , T^r_{ij}. (Note that the first two terms have been enlarged by ten.)

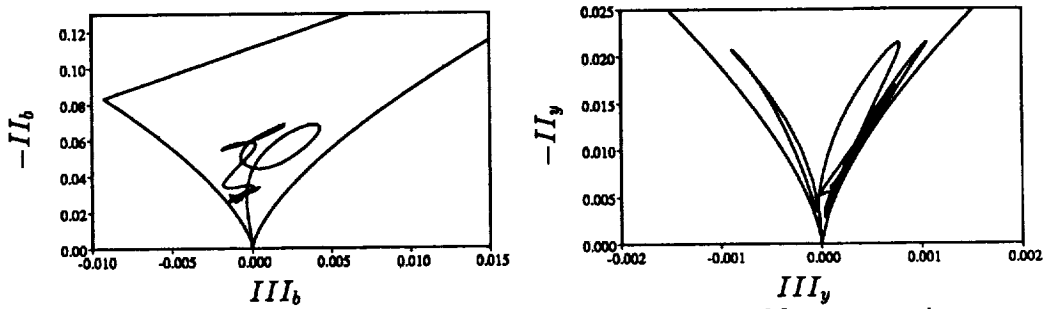

FIGURE 14. Invariant maps for case D' for (a) the Reynolds stress anisotropy tensor, and (b) the structure dimensionality anisotropy tensor.

for these cases. However, in the later stages of the simulations, nonlinear effects begin to grow.

For the case with a moderate aspect ratio and Rossby number, the nonlinear cascade is reduced and then reestablished and finally displays large amplitude oscillations. This behavior may be related to the resonant collapse phenomenon observed in experiments of the elliptic streamline flow. The turbulent kinetic energy for this case shows algebraic rather than the exponential growth predicted by the linear theory.

One difficulty with these simulations is that the large scales grow in energy and eventually dominate the flow. As a consequence, the computational box size becomes inadequate and the simulations must be stopped. Since the long time behavior of the turbulence is of interest, a means of extending the simulations further in time is needed, and this is one of the goals for future work.

The elliptic streamline flow presents a challenging case for turbulence modelers. The Reynolds stresses display complex behavior and they oscillate as they grow.

The Reynolds stresses and their budgets have been computed during the course of each simulation, but they have not been analyzed in detail nor compared to predictions of turbulence models.

The elliptic streamline flow is a very interesting case. It is related to important flows in engineering and geophysical applications, and it displays a wide range of behavior that is yet to be understood. There are many tasks to be done in continuing this work. Further simulations are needed to better map out the parameter space. Upon identifying interesting cases, such as case D in the current work, simulations on larger grids should be done. In order to carry the simulations further in time, large-eddy simulations should be used so that the small length scales do not have to be resolved and more of the computational grid can be used to capture the large length scales. Finally, a detailed analysis of the Reynolds stresses and their budgets, and a comparison with turbulence models is needed.

Acknowledgements

The authors thank Dr. R. S. Rogallo for use of his program, help extended during modification, and numerous other discussions.

REFERENCES

BARDINA, J., FERZIGER, J. H., & REYNOLDS, W. C. 1983 Improved turbulence models based on large-eddy simulation of homogeneous, incompressible turbulent flows. Thermosciences Division Report TF-19, Stanford University, Stanford, California.

BAYLY, B. J. 1986 Three dimensional instability of elliptic flow. *Phys. Rev. Lett.* **57**, 2160–2171.

BENOIT, J.-P. 1992 Etude expérimentale et théorique d'une turbulence homogéne soumise à des effets couplés de rotation et de déformation plane. Ph.D. thesis, L'Ecole Central de Lyon, France.

LANDMAN, M. J. & SAFFMAN, P. G. 1987 The 3-D instability of strained vortices in a viscous fluid. *Phys. Fluids.* **30**, 2339–2342.

LUMLEY, J. L. 1978 Computational modeling of turbulent flows. *Advances in Applied Mechanics.* **18**, 123–173.

LUNDGREN, T. S. & MANSOUR, N. N. 1991 Transition to turbulence in an elliptic vortex. *Annual Research Briefs.* Center for Turbulence Research, NASA Ames/Stanford Univ.

MALKUS, W. V. R. 1989 An experimental study of global instabilities due to the tidal (elliptical) distortion of a rotating elastic cylinder. *Geophys. Astrophys. Fluid Dyn.* **48**, 123–134.

MALKUS, W. V. & BERRY, M. E. 1988 Order and disorder in planetary dynamos. *Summer Study Program in Geophysical Fluid Dynamics*, (eds. W. V. Malkus and M. E. Berry).

MANSOUR, N. N., CAMBON, C. & SPEZIALE, C. G. 1991 Single point modeling of initially isotropic turbulence under uniform rotation. *Annual Research Briefs.* Center for Turbulence Research, NASA Ames/Stanford Univ.

PIERREHUMBERT, R. T. 1986 Universal short-wave instability of two-dimensional eddies in an inviscid fluid. *Phys. Rev. Lett.* **57,** No. 17, 2157–2159.

REYNOLDS, W. C. 1987 Fundamentals of turbulence for turbulence modeling and simulation. *Lecture Notes for Von Karman Institute*, April 1987.

REYNOLDS, W. C. 1989 Effects of rotation on homogeneous turbulence. *10th Australian Fluid Mechanics Conference,* University of Melbourne, Australia, December 1989.

ROGALLO, R. S. 1981 Numerical experiments in homogeneous turbulence. NASA Technical Memorandum 81315.

ROGERS, M.M., MOIN, P. & REYNOLDS, W.C. 1986 The structure and modeling of the hydrodynamic and passive scalar fields in homogeneous turbulent shear flow. Thermosciences Division Report TF-25, Stanford University, Stanford, California.

SPEZIALE, C. G. & MAC GIOLLA MHUIRIS, N. 1989 On the prediction of equilibrium states in homogeneous turbulence. *J. Fluid Mech.* **209,** 591–615.

WALEFFE, F. 1990 The three-dimensional instability of strained vortices. *Phys. Fluids A.* **2,** 76–80.

WIDNALL, S. E., BLISS, D. B., & TSAI, C.-Y. 1974 The instability of short waves on a vortex ring. *J. Fluid Mech.* **66,** 35–47.

C-5